White Rose Research Online

eprints@whiterose.ac.uk
https://eprints.whiterose.ac.uk
Universities of Leeds, Sheffield and York

Deposited via The University of York.

White Rose Research Online URL for this paper:
https://eprints.whiterose.ac.uk/id/eprint/239033/

Version: Accepted Version

Article:
HILL, JON, Vila-Concejo, Ana and LEE, KATIE (2026) Toward a digital twin of the Great Barrier Reef:Impact of extreme model resolution on tidal simulations. Ocean Modelling. 102723. ISSN: 1463-5003

https://doi.org/10.1016/j.ocemod.2026.102723

Reuse
This article is distributed under the terms of the Creative Commons Attribution (CC BY) licence. This licence allows you to distribute, remix, tweak, and build upon the work, even commercially, as long as you credit the authors for the original work. More information and the full terms of the licence here:
https://creativecommons.org/licenses/

Takedown
If you consider content in White Rose Research Online to be in breach of UK law, please notify us by emailing eprints@whiterose.ac.uk including the URL of the record and the reason for the withdrawal request.

UNIVERSITY OF LEEDS
University of Sheffield
UNIVERSITY of York

Highlights

Toward a digital twin of the Great Barrier Reef: impact of extreme model resolution on tidal simulations

Jon Hill, Ana Vila-Concejo, Katherine C. Lee

- Digital twins utilise extremely high resolution data and numerical models.
- Very high resolution (5 m) models capture the filling and emptying of lagoons.
- Resolution-dependant simulations has implications on simulating larval dispersal.
- Future digital twins need to account for both data and model resolution.

Toward a digital twin of the Great Barrier Reef: impact of extreme model resolution on tidal simulations

Jon Hill[a,*], Ana Vila-Concejo[b,c] and Katherine C. Lee[a]

[a]Department of Environment and Geography, University of York, UK
[b]Geocoastal Research Group, School of Geosciences, University of Sydney, Australia
[c]Marine Studies Institute, Faculty of Science, University of Sydney, Australia

ABSTRACT

Coral reefs are topologically complex environments with a large variation over small spatial-scales. The availability of high resolution data (metre-scale) to study these environments has increased rapidly such that many researchers are actively engaged in creating a 'digital twin' of these environments to aid protection and management. However, as with any model, a digital twin will only be as useful as the data used to create it. Previous numerical modelling work on coral reefs has been carried out at a range of resolutions from tens to thousands of metres, but to date there has been no comprehensive study on the impact of extreme model resolution at metre-scale. Here, we simulate the Capricorn Bunker region of the GBR in a high resolution, multi-scale hydrodynamic model using grid scales of 20,000 m to 5 m and compare that to the models with minimum grid scales of 250 m and 50 m. It is shown that the observable physical processes are best simulated at extremely high resolutions, though the intermediate resolution model performs well also. The low resolution model, whilst using a resolution comparable to a number of previous studies, does not sufficiently capture local-scale processes, such as phase eddies. Numerical models play a vital role in creating a digital twin of coastal seas as they contain the mathematical representation of the biophysical and chemical processes present but are currently at a coarser resolution than satellite and bathymetric data on which digital twins could be based. Bridging this resolution gap remains a challenge.

1. Introduction

The recent increase of high-resolution bathymetric data, including derived from LiDAR surveys, opens up a number of opportunities for refining coastal ocean models (Kutser et al., 2020). This advancement of high resolution data holds the potential to begin constructing 'digital twins' of coastal environments (Tzachor et al., 2023). Such digital twins, capable of mirroring the real-world dynamics of coastal process with two-way automated data flow between the numerical (digital) and the real versions, would be valuable tools for informed planning and management of human activities within the coastal zones (Hazeleger et al., 2024). The flow of information between these digital representations and their real-world counterparts could be facilitated through automated extraction of flow patterns from high-resolution satellite imagery, such as PlanetScope's 3 x 3 m resolution (e.g. Tlhomole et al., 2025), enabling both instantaneous model validation and continuous data assimilation for performance tuning, for example. The application of such digital twins includes assessing the environmental impacts of anthropogenic activities and management of Marine Protected Areas, especially in sensitive areas, such as coral reefs (Durden, 2025).

Coral reef ecosystems present a challenge for numerical modelling and creating a digital twin. These environments are inherently complex, exhibiting a large degree of heterogeneity across various spatial scales (Torres-Pulliza et al., 2020). Accurately simulating hydrodynamic processes, such as tidal propagation, is challenging within such heterogenous settings and has long known to be so (Bode et al., 1997). Therefore, the resolution employed, both in the model and of any associated data, becomes important in order to capture this spatial heterogeneity (Saint-Amand et al., 2023). Previous studies have shown tidal phenomenon have clear impacts of both coral and fish larval dispersal and retention. The flow patterns within these ecosystems directly influence a number of ecological processes, including coral larval dispersal (Andutta et al., 2012), fish larval dispersal (Burgess et al., 2007; Booth et al., 2000), nutrient transport (Wolanski et al., 1988), and the distribution of dissolved oxygen (Gruber et al., 2017). A number of studies have examined the role tidal currents have played on coral larval retention on the Great Barrier Reef (Andutta et al., 2012; Wolanski et al., 2024). In particular, the phenomenon of 'sticky waters' where mesoscale eddies trap larvae

ORCID(s): 0000-0003-1340-4373 (J. Hill); 0000-0003-4069-3094 (A. Vila-Concejo); 0000-0002-8922-3926 (K.C. Lee)

behind reefs (Wolanski and Spagnol, 2000) are thought to be a key factor. Other studies show that this is a function of a dense reef matrix (Andutta et al., 2012). The formation of tidal eddies have been implicated as a major driver of fish larval retention and dispersal on the GBR (Booth et al., 2000; Burgess et al., 2007). In particular, 'phase eddies' (Black and Gay, 1987) where the unsteady tidal flow generates eddies in the lee of islands at both the flood and ebb phases of the tidal cycle, are thought to be major factor of retention of passive larva and eggs by trapping them in the eddy such that the reversal of flow bring them back over the parent reef (Burgess et al., 2007). Accurate models of hydrodynamics, preferably augmented by digital twinning techniques, are therefore essential for predicting the connectivity between reef habitats, informing conservation strategies aimed at maintaining genetic diversity and promoting reef resilience (Elmhirst et al., 2009; Williamson et al., 2016).

Robust hydrodynamic models, and hence digital twins, can therefore serve as a vital tool for bridging the gap between physical processes and ecological outcomes, providing crucial insights on these ecologically significant ecosystems (Tzachor et al., 2023). Previous investigations have demonstrated the necessity of resolutions ranging from approximately 250 m to 500 m to adequately represent ocean and tidal currents in reef areas (Saint-Amand et al., 2023), which can then explain differences in high resolution tidal simulations (e.g. Mawson et al., 2022) vs. lower resolution simulations (e.g. Harker et al., 2019). Model resolution has long been known to be a fundamental issue in representing physical processes in ocean and coastal models, with unstructured meshes one of the possible solutions (Greenberg et al., 2007). However, studies have yet to quantify the impact of ultra-high resolution simulations, specifically those operating at sub-100 m scales, which is the resolution that satellite imagery and bathymetric data can now be readily obtained (McCarthy et al., 2022), though models are being developed which can simulate at this scale (Wagner et al., 2025). A digital twin that can extract information such as flow vectors (Tlhomole et al., 2025) from such high resolution imagery can then be integrated into a digital twin framework via data assimilation methods (Alsulaiman et al., 2025). This resolution gap is critical, as the scale at which processes are resolved directly influences the accuracy of predictions, particularly when assessing environmental change or understanding secondary processes, be they large-scale phenomena like sea-level rise, localized interventions such as coastal engineering projects, or assessing ecological impacts, such as larval dispersal.

Before creating digital twins of complex heterogenous environment such as coral reefs, there is therefore a need to evaluate the impact of extreme model resolution on hydrodynamics. In this context, 'extreme' is defined as metre-scale resolution within a broader regional-scale domain. This necessitates the adoption of unstructured mesh models, which offer the flexibility to spatially vary resolution, concentrating computational effort in areas of particular interest (e.g. Zhang et al., 2023). Previous work has examined the impact of extreme resolution on coral reef hydrodynamics, but generally in a limited domain size and using semi-idealised bathymetric data with CFD-type models (Osorio-Cano et al., 2018; da Silva et al., 2020; Watanabe et al., 2023). However, there are issues with depth-averaged assumptions, such as the hydrostatic assumption, with respect to vertical velocities (e.g. Rogers et al., 2015), and then computational limits when moving to three dimensions and using non-hydrostatic models. Coral reefs, with their inherent spatial variability, pose a significant challenge for digital twin development, yet they are also crucial hotspots of marine biodiversity facing unprecedented threats (Hoegh-Guldberg et al., 2007). The rate of coral reef degradation, with approximately 10% already lost and a further 60% at risk, underscores the need of developing robust predictive tools (Eddy et al., 2021). These ecosystems therefore present an ideal, albeit challenging, test-bed for evaluating the impact of model resolution within a digital twin framework.

This study uses a highly multi-scale numerical model to simulate tidal dynamics within the Great Barrier Reef (GBR). We undertake a validation of the model against observational tidal gauge data across three distinct model resolutions. Subsequently, we perform a detailed comparative analysis of tidal dynamics, employing a range of quantitative metrics, focusing on a single atoll reef, One Tree Reef, for which exceptionally high-resolution (0.25 m) bathymetric data is available (Talavera et al., 2021; Harris et al., 2023). Previous research investigating physical processes at One Tree Reef have focused on wave energy dissipation (Duce et al., 2022; Perris et al., 2024); sediment transport and geomorphology (Harris et al., 2014; Talavera et al., 2021; Vila-Concejo et al., 2022); wind-driven circulation (Frith and Mason, 1986; Burgess et al., 2007); and tides (Wilson, 1985; Ludington, 1979), but no study has simulated tides with high resolution bathymetric data.

1.1. Study site

One Tree Island (OTI) and Reef (OTR) are situated in the Capricorn Group (Fig. 1), in the southern Great Barrier Reef (GBR) (Davies et al., 1976). OTR spans and area of around 40,000 square metres, including a 5.5 km by 3 km reef and a small, vegetated, shingle cay located in the southeastern corner of the platform (Bauder et al., 2023). The lagoon

is entirely rimmed by reef crest. The reef contains a main lagoon in the centre of the reef, comprising of depths that vary between 0.75-20 m, with smaller lagoonal areas adjacent. The main lagoon is relatively shallow, with a maximum ponded depth of around 6 m at the northern edge where fine mud dominates the sediment. It contains a number of small patch reefs that reach the ponded surface. At the shallower southern and eastern edges, the lagoonal sediment is dominated by coarse sand. (Kosnik et al., 2015). The tidal dynamics at One Tree are governed by the semidiurnal principal lunar (M_2) and solar (S_2) components with a diurnal divergence (ponding effect) as the lagoon is separated from the ocean (Wilson, 1985) by the reef crest. The island therefore experiences a primary tidal pattern that comprises two high and low tides per day, with a tidal range of approximately 3.4 m (Hatcher and Frith, 1985), but becomes almost diurnal in nature during neap periods. The tidal patterns causes the reef platform encompassing OTR to be exposed for 5-6 hours at low spring tide which means the lagoon has limited exchange with the open ocean for significant parts of the tidal cycle (Ludington, 1979; Wilson, 1985; Harris et al., 2014).

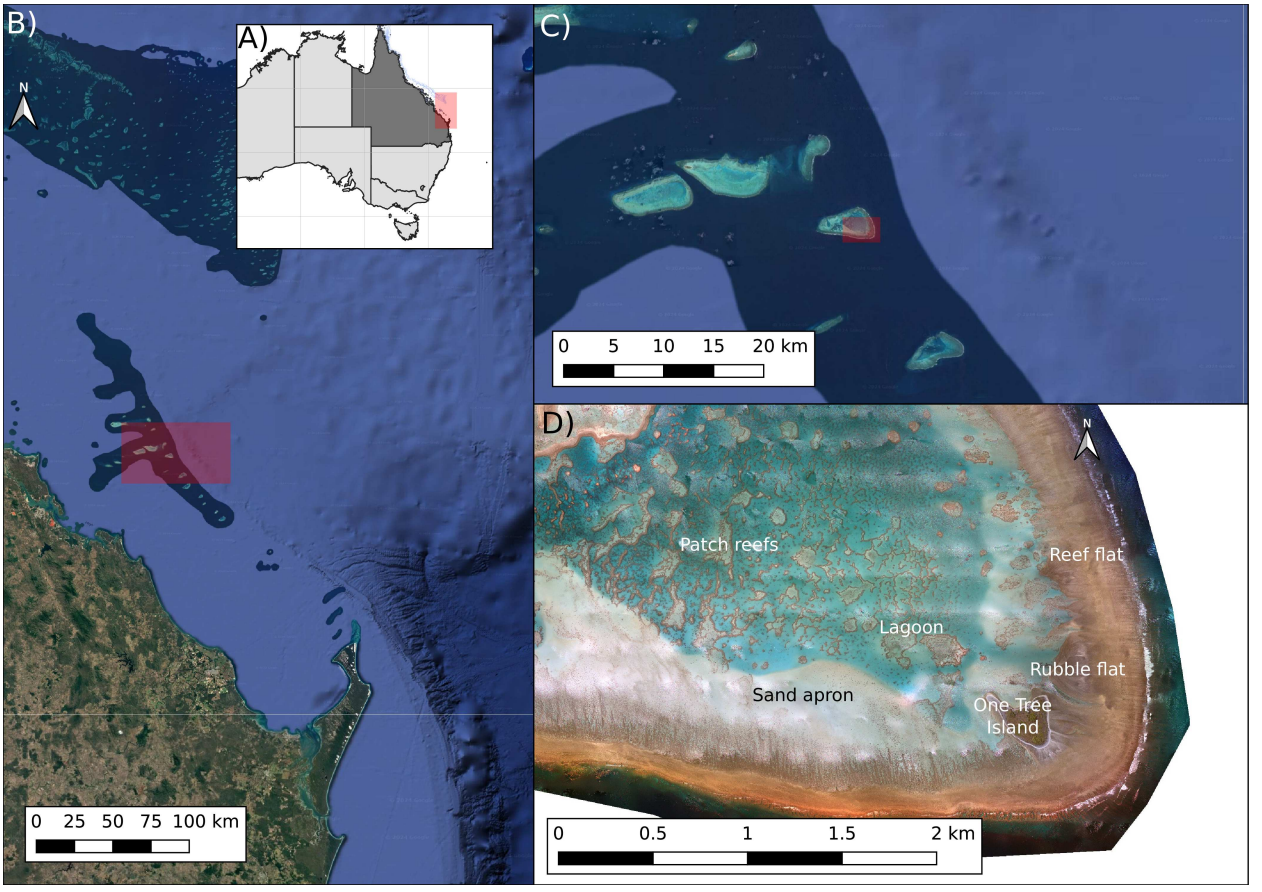

Figure 1: Location of One Tree Reef, within the Great Barrier Reef's Capricorn Group islands. A) shows the Australian coastline, with blue showing the reef locations. The red square then shows the location of B). Panel B) shows the Capricorn Group of atoll islands. Panel C) shows One Tree Reef (location show by the red square in B). Panel D shows a zoom-in of One Tree Island with various geomorphological features highlighted. Panel D is the RGB part of the LiDAR data described in Talavera et al. (2021); Harris et al. (2023).

2. Methods

2.1. Model details and set-up

Coastal models that represent coastal and oceanic regions can be used to predict any alterations in tidal cycles due to changes in infrastructure, coastal alterations or sea level change (e.g. Baker et al., 2020; Lee et al., 2022; Mawson et al., 2022). In this work, *thetis* was employed, which is a finite element based coastal ocean model that implements

both 2D and 3D equations (Kärnä et al., 2018). *thetis* solves the non-conservative form of the non-linear shallow water equations:

$$A(H)\frac{\partial \eta}{\partial t} + \nabla \cdot (\tilde{H}\mathbf{u}) = 0, \tag{1}$$

$$\frac{\partial \mathbf{u}}{\partial t} + \mathbf{u} \cdot \nabla \mathbf{u} + f\mathbf{u}^{\perp} + g\nabla\eta + \nabla\frac{p_a}{\rho_0} = -\frac{\tau_b}{\rho\tilde{H}} + \nabla \cdot (\nu(\nabla\mathbf{u} + \nabla\mathbf{u}^T)), \tag{2}$$

where $A(H)$ is the wetting and drying formulation (see below), η is the water elevation, H_d is the total water depth, ν is the kinematic viscosity of the fluid, and $\mathbf{u}$ is the depth-averaged velocity vector. The Coriolis term is represented as $f\mathbf{u}^{\perp}$, where $\mathbf{u}^{\perp}$ the velocity vector rotated counter-clockwise over 90^o. In turn, $f = 2\Omega\sin\zeta$ with Ω corresponding to the angular frequency of the Earth's rotation and ζ the latitude. Note that the continuity equation (eq. 1) has modified following Kärnä et al. (2011) such that $\frac{\partial \eta}{\partial t} + \frac{\partial \tilde{h}}{\partial t} = A(H)\frac{\partial \eta}{\partial t}$, where $\tilde{h}$ is defined by:

$$\begin{aligned} \tilde{h}(\eta, h) &= h + f(H), \\ f(H) &= \frac{1}{2}(\sqrt{H^2 + \alpha^2} - H) \end{aligned} \tag{3}$$

such that during low tide, areas of the reef will be exposed. Here, $f(H)$ ensures redefined total depth remains positive, via the wetting and drying parameter (α), η is the free surface height and h is the original static bathymetry depth. The wetting and drying α parameter was set as a function of element size and slope and could vary between 0.1 and 75. The smallest values are used where the mesh resolution is high and the slope is low and the highest values used where the mesh is coarse and the slope is high. As such α is similar to threshold depth parameters used in thin-layer wetting and drying methods and determines the remaining water layer depth (Kärnä et al., 2011). Bed shear stress (τ_b) effects are represented through the Manning's n formulation as:

$$\frac{\tau_b}{\rho} = gn^2\frac{|\mathbf{u}|\mathbf{u}}{{H_d}^{\frac{1}{3}}} \tag{4}$$

For time-stepping, a second-order DIRK22 discretisation was used with a constant time step which varied depending on the smallest grid-scale used (see below).

The models were implemented following the Galerkin finite element discretisation (DG-FEM), using the P1DG-P1DG velocity-elevation finite element pair (Angeloudis et al., 2018; Baker et al., 2020). Discretised equations are solved using a Newton nonlinear solver algorithm via the PETSc library (Balay et al., 2001).

2.2. Mesh Generation and Model Construction

The mesh needs to be of sufficient extent to avoid boundary condition issues, whilst containing enough resolution to resolve any areas of complex bathymetry or coastal geomorphology, but also, in this case, the high resolution bathymetric data on OTR. As *thetis* is a finite-element model it can readily use spatially-varying mesh resolution, allowing higher resolution near areas of interest, with coarse resolution away from the site (e.g Hill et al., 2023). Here, we created three meshes which are identical except the edge-length metric employed in the area around OTR. Bathymetric and topographic data came from two sources. The GBR bathymetric data of Beaman (2010), and the LiDAR survey carried out over OTR as described in Talavera et al. (2021) and Harris et al. (2023). The Beaman (2010) data were resampled to 400 m and 100 m resolution in UTM56 projection space. The OTR data was resampled to 5 m resolution in UTM56 projection space, with small amounts of missing data filled in via linear interpolation.

The mesh boundaries are created from bathymetric/topographic data by creating a contour at a set height to create the 'landward' boundary, and joining that via a smooth arc to create the open boundary of the model. The contour used here is the +5 m contour. The contour was then modified by removing small 'holes' in the mesh of less than 3000 m circumference. The contour was also modified to remove narrow bays or other coastal features that contains fewer than two elements width. An external forced boundary was then added between -22.53°latitude, 150.78°longitude at the

northern extent to -25.93°latitude, 153.18°longitude on the southern edge, going out around 150 km from the modern coastline. Processing and contour creation were carried in QGIS (QGIS.org, 2020). GIS data were converted to meshes via *qmesh* (Avdis et al., 2018) and *gmsh* (Geuzaine and Remacle, 2009).

Mesh resolution for the model was determined by five factors: water depth, $\mathcal{H}_b$; water depth from the OTR high resolution bathymetric data, $\mathcal{H}_o$; distance from the 'landward' boundary, $\mathcal{H}_{lb}$; distance from forced boundary $\mathcal{H}_{ob}$; and the distance from OTR, $\mathcal{H}_{dm}$ or $\mathcal{H}_{dh}$. The final mesh resolution, $\mathcal{H}$, is the minimum of the factors:

$$\mathcal{H} = \min\left(\mathcal{H}_b, \mathcal{H}_o, \left[\mathcal{H}_{dh} \middle| \mathcal{H}_{dm}\right], \mathcal{H}_{lb}, \mathcal{H}_{ob}\right) \tag{5}$$

Bathymetric/topographic control was governed by:

$$\mathcal{H}_b = 20000 \frac{\exp\left(\frac{(-b-165)}{50}\right)}{\exp\left(\frac{(-b-165)}{50}\right) + 1} \tag{6}$$

where b is the topographic height. A different form was used with the high resolution bathymetric data of OTR:

$$\mathcal{H}_o = 0.4b^2 + 0.1b + 5 \tag{7}$$

Note that the high resolution bathymetric data is only defined on One Tree Reef and is not defined elsewhere, restricting the application of $\mathcal{H}_o$ to One Tree Reef only.

Resolution as a function of distance from OTR was governed by creating a polygon over OTR where distance was set to zero. The *gdal* proximity function (GDAL/OGR contributors, 2025) was then used to create a raster which contained the distance (in metres) from that polygon area. Mesh resolution was then calculated using:

$$\mathcal{H}_{dh} = \frac{D}{6} + 20.0 \tag{8}$$

where D is the distance from the polygon. For the medium resolution mesh, $\mathcal{H}_d$ was:

$$\mathcal{H}_{dm} = \frac{D}{6} + 50.0 \tag{9}$$

and for the low resolution mesh, this metric was not included.

The final two resolution metrics were constructed in the same way, but using different parameters. For the 'landward' boundary resolution, $\mathcal{H}_{lb}$, increased from 500 m to 20 km linearly to a distance of 50 km with the first 1000 m away from the boundary fixed at 500 m resolution. For the open boundary the resolution, $\mathcal{H}_{ob}$, increased from 2 km at the boundary to 20 km away from the boundary at a distance of 50 km, with the nearest 6 km fixed at 2 km resolution.

Mesh resolution therefore varies from 20 km in the Pacific Ocean to either 5 m, 50 m or around 250 m around OTR (Fig. 2). The three meshes can were then constructed using the correct components of the overall mesh metric (Table 2.2). The meshes contained between 1.1 million to 100,000 elements. Henceforth, the three meshes will be referred to as HR (high resolution), MR (medium resolution) and LR (low resolution).

All bathymetric/topographic datasets were interpolated onto the mesh using bilinear interpolations, with blending of different data carried out using the HRDS package (Hill, 2019). All models used three bathymetric datasets: a 400 m version of Beaman (2010) which covered the whole domain; a 100 m version of Beaman (2010) covering the central part of the domain, and a 5 m version of the Talavera et al. (2021) LiDAR data over OTR, but are interpolated linearly onto the mesh. All bathymetric data were projected to UTM56 coordinate reference system and use the same datum. Due to the mesh resolution the models can 'see' different geomorphological features, such as spur and grooves on the windward side of One Tree Island, or the various channels that cut across the reef front (Fig 2).

All models used the same numerical parameters, forcing datasets and bathymetric/topographic data. Models were forced using TXPO version 9 (Egbert and Erofeeva, 2002) starting from November 22, 2022 at midnight UTC. The

Table 1
Definition of the final mesh metric used in the three meshes for low, medium and high resolution models.

Mesh	Mesh metric	Resolution range (m)	No. of elements in mesh
LR	$\mathcal{H} = \min\left(\mathcal{H}_b, \mathcal{H}_{lb}, \mathcal{H}_{ob}\right)$	5 to 20,000	1,166,124
MR	$\mathcal{H} = \min\left(\mathcal{H}_b, \mathcal{H}_{dm}, \mathcal{H}_{lb}, \mathcal{H}_{ob}\right)$	50 to 20,000	122,290
HR	$\mathcal{H} = \min\left(\mathcal{H}_b, \mathcal{H}_o, \mathcal{H}_{dh}, \mathcal{H}_{lb}, \mathcal{H}_{ob}\right)$	250 to 20,000	100,322

only minimal change between models (except the mesh) was a change in the model timestep from 180 s for the LR model to 90 s for the MR and HR models. Output was stored every 15 minutes for subsequent analysis. Due to the long run times required for the HR model these models were run for 16 days plus an additional 2 days spin-up. The MR and LR models were run for 30 days plus an additional 2 days spin-up. All model parameters are detailed in the supplementary information.

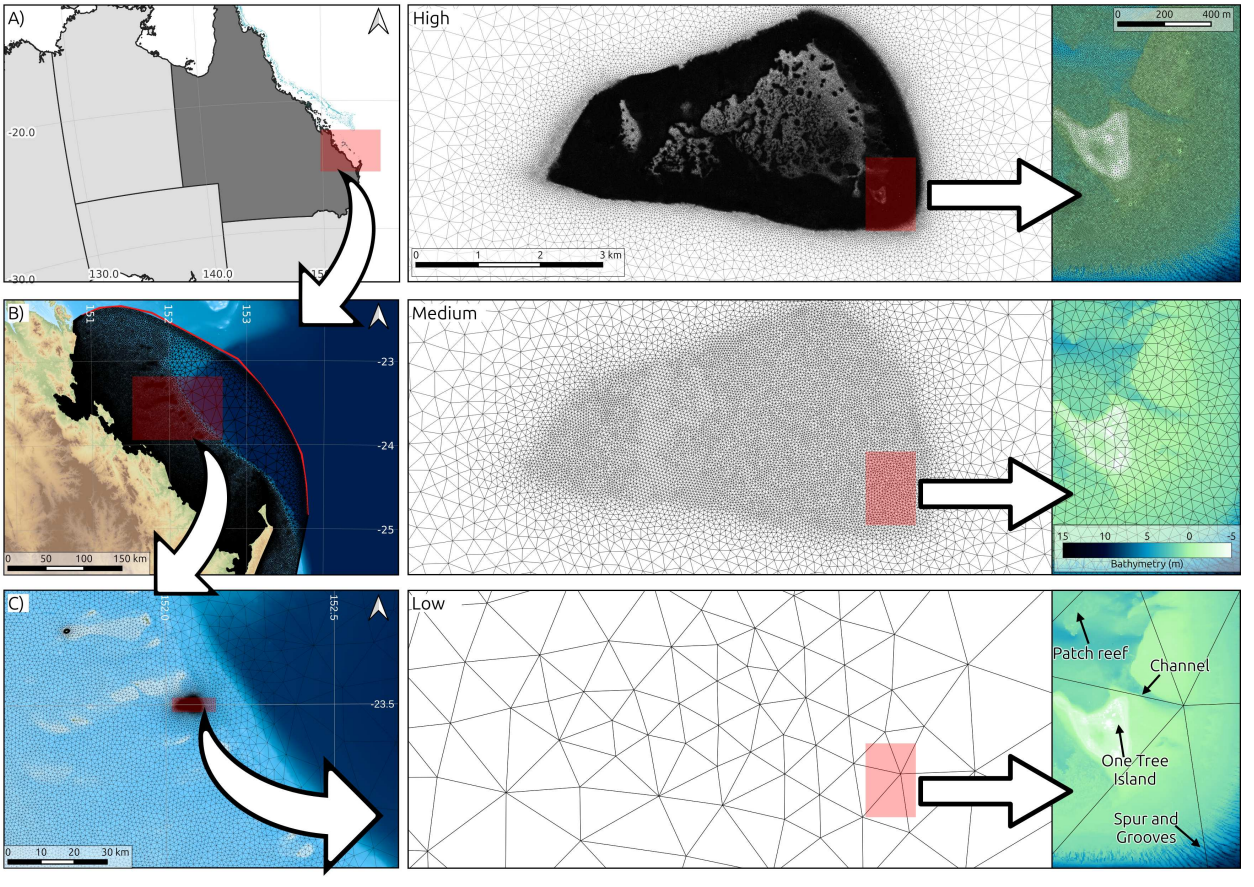

Figure 2: Overview of the model domain and mesh (left; A and B, C), with close up of the OTR areas (centre and right). The central panels show the mesh for the HR (top), MR (centre) and LR (bottom) simulations around OTR, with a close-up around the One Tree Island (right panels). Note that the high resolution mesh can resolve the various labelled geomorphological features, whereas the MR mesh will resolve some and the LR mesh will smooth these features or not resolve at all.

2.3. Particle tracking

In order to establish the impacts of model resolution on physical processes around OTR, offline Lagrangian particle tracking was employed as a method of estimating flushing times of the lagoon. Here, a modified version of *parcels* (Delandmeter and van Sebille, 2019) was used where, rather than using gridded input normally required, the velocity

Table 2
Various tidal model performance metrics split by tidal constituents. The first two rows are based on the error metric of Cummins and Thupaki (2017), with relative error calculated using the mean measured amplitude. The Pearson's *r* and p-value were calculated using the standard methods.

	M_2	S_2	K_1	O_1
Error	0.0715 m	0.0205 m	0.0077 m	0.0061 m
Relative error	7.38%	5.96%	2.98%	4.56%
Pearson's *r*	0.9719	0.9271	0.8212	0.8966
p-value	$\ll 0.001$	$\ll 0.001$	$\ll 0.001$	$\ll 0.001$

at each particle location was evaluated on the finite element function on the unstructured mesh. No horizontal diffusion of random walk algorithms were applied. Linear interpolation in time was used between model outputs. Moreover, the particles were held in position when water elevation was lower than the bathymetric height so particles did not move when 'dry'. A set of 10,000 random locations was generated within the OTR area and used as starting locations for all particle simulations. The particle tracking used a 4th order Runge-Kutta timestepping algorithm, with a timestep of 120 seconds. Outputs (particle positions and time) were stored every 240 seconds.

Particles were released and tracked for 48 hours. A total of 32 release times were used for each model; 16 during the spring tide period and 16 during the neap part of the tidal cycle. Release times started at 314,880 seconds (3.64 days; spring tide) or 1,076,400 seconds (12.46 days; neap tide) after the model start time and were 10,000 seconds apart until 16 releases had been carried out. To establish the flushing rate, the number of particles were counted within the OTR area at each particle tracking output step, including those that had re-entered the domain. The mean number of particles per step was then calculated across the 16 spring tide release points and the 16 neap tide release points. To compare the effects of model resolution on the lagoon flushing, two statistical tests were carried out. First, an ANOVA with Tukey post-hoc HSD was carried out on the 16 groups at 5 hour intervals. This therefore computes any statistical difference in the flushing rates at a static point in time across the three models resolutions. Second, a Functional Data Analysis ANOVA was carried out which examines statistical difference in the groups of lines as a set of whole time series. Here, we used the R package *fdANOVA* (Górecki and Smaga, 2019) using a b-spline basis function. We report the results of the L2N test and the TRP (Test Random Projection) using 30 Gaussian projections with 1000 permutations each. This test produces three p-values based on different statistical tests.

The pathways for each particle were also tracked and the location of where they crossed the OTR outline was noted as an inflow or outflow point. Multiple events were counted for each track. To count the number of tracks crossing each location a Kernel Density Estimation function using a quartic kernel shape was applied to the exit or entry points with a radius of 25 m and stored in a raster with 5 m pixel size.

3. Results

3.1. Model Validation

To demonstrate the model is capable of replicating the tidal system in the area we validated the model against 23 tide gauges in the region using the MR and LR models as they could be run for a full 30 day tidal cycle; note that only the One Tree Islet tidal gauge is located in the region where the resolution is altered. The validation shows good agreement for the amplitude four major tidal components in the region (Table 2) using a mix of regression and the error metric proposed by Cummins and Thupaki (2017). The model can accurately replicate the tidal elevation of all the tide gauges in the region (Fig. 3). The change in resolution does not alter the comparison, except for the One Tree Islet gauge station, as expected.

Model resolution has a clear impact on correctly simulating the ponding effect on OTR. Wilson (1985) showed that there is a time lag in water height from outside the lagoon, the northern edge of the lagoon and to the cay on the southern side and the centre of the lagoon. This results in the water elevation at the cay lagging behind the northern edge of the lagoon by up to one hour, which in turn lags behind the elevation outside the lagoon (Fig. 4). The LR model did not capture this observed phenomenon, with the tidal elevation at the cay slightly lower than, but not out of phase of, the outer lagoon or the outer reef locations. Both the MR and HR simulations showed this phase lag, but it was much more pronounced in the HR model (Fig. 4C). This shows the clear difference, at a local scale, of model

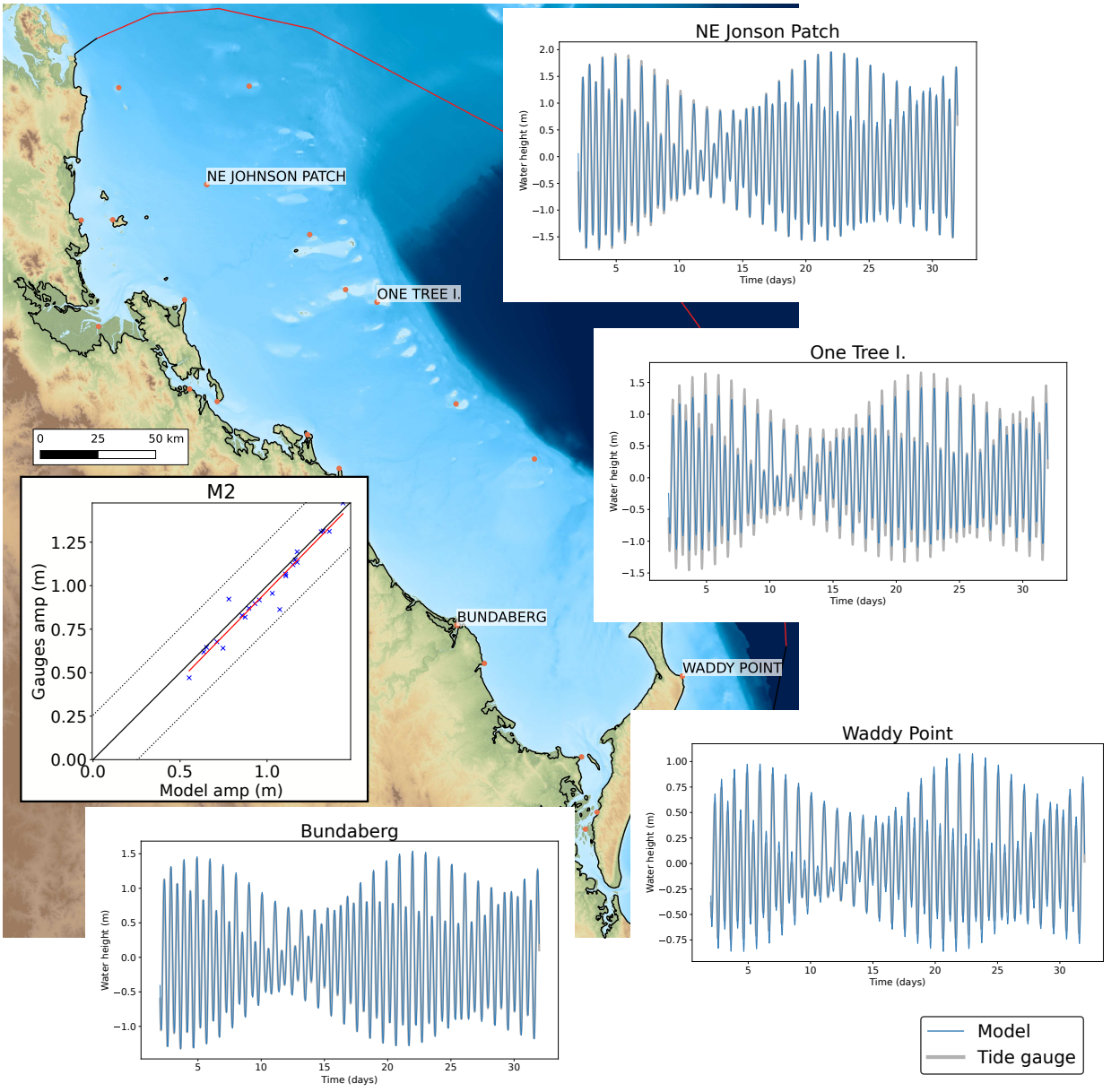

Figure 3: Verification of the tidal model at medium resolution with tide gauges within the domain. The cross plot shows the correlation of the M_2 amplitude of the model gauges (x-axis) against gauge data (y-axis). The red line indicates the line of best fit, with the solid black indicating the 1:1 relationship and the dotted line the standard deviation of the measured amplitudes. Four example tidal gauges are show from across the domain (see central map for locations), which show the theoretical tide at the location in grey, with the modelled tide overlain in blue.

resolution with higher resolution simulations successfully capturing the filling and emptying of the lagoon over a tidal cycle.

3.2. Impact of resolution on hydrodynamics

The differences in flow as a function of resolution are clearly seen in and around OTR. During the spring tide phase in the HR model (Fig. 5) there is a clear eastward jet of fast flowing water that arcs along the southern side of OTR and then turns north on the eastern side of the reef at low tide (ebb, with predominantly easterly flow). This jet is present in all three simulations, but the flow magnitude and direction are different. The LR model shows a weakly

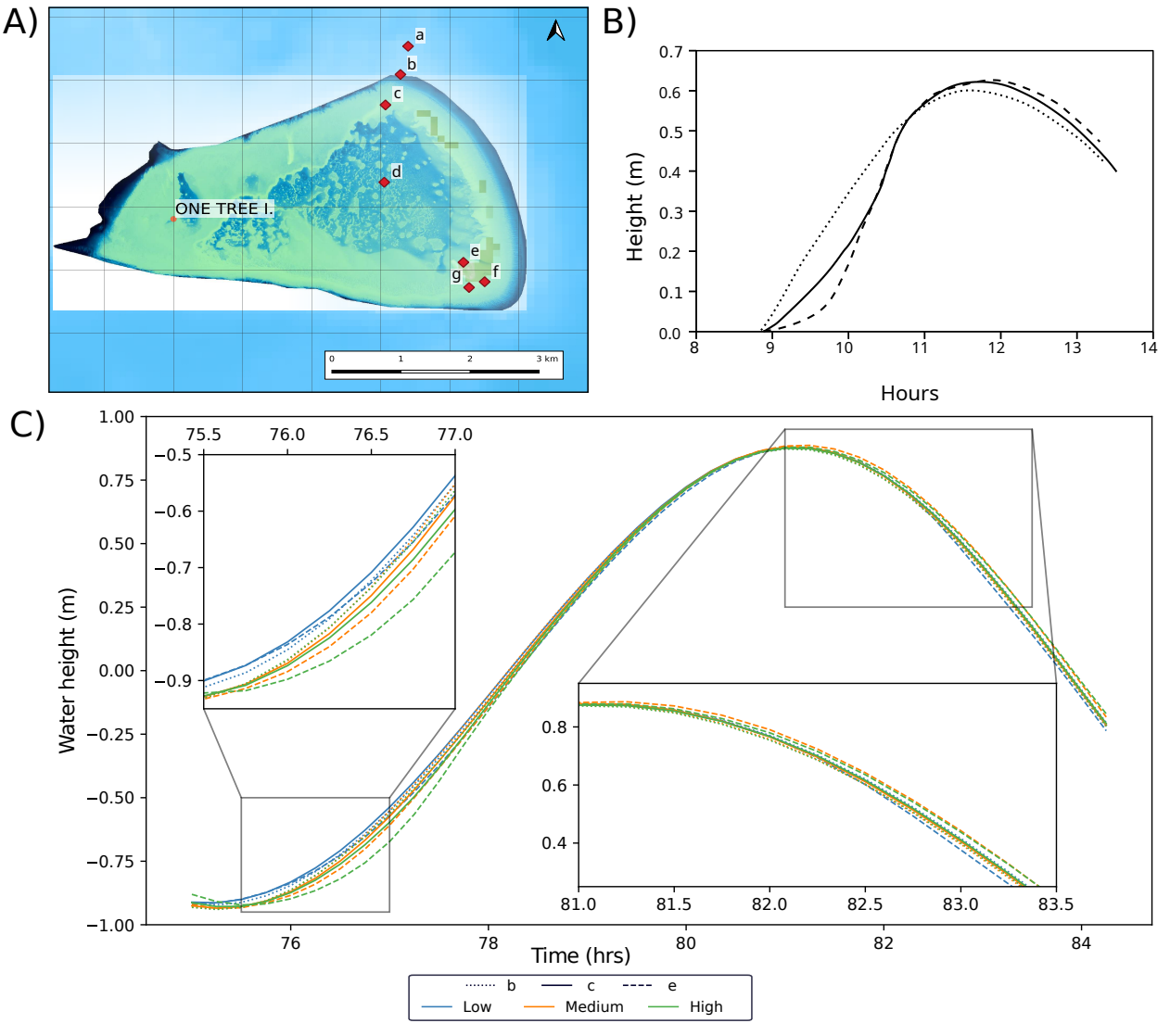

Figure 4: Location of points (b, c and e) around OTR (panel A) where the ponding effect can be measured. Points are those used by Wilson (1985) to demonstrate the lagged filling and emptying of the lagoon at OTR (panel B; after Wilson (1985)). The linetype indicates the gauge location (dotted: gauge b, solid: gauge c, dashed: gauge e) and colour denotes the model resolution (low: blue, medium: orange, high: green). Two insets in panel C show the lag phenomenon at rising (left) and falling (right) tide respectively.

defined jet travelling to around 2 km east of the island before becoming more diffuse in a north-easterly direction. The jet increases in strength and definition as resolution increases, turning northward around 4-5 km from the island. Similarly, at rising tide a clear eddy is seen on the south-eastern corner of OTR, near OTI, which concentrates flow and produces a high velocity flow eastwards to the south of the reef rim (HR model). On the LR model this high velocity flow is concentrated on OTI itself, rather than off the southern edge of the reef, and is lower in magnitude. The MR model shows a clear eddy, but lacks the definition of the HR model and also has a lower peak velocity. Finally, at high tides, the southern edge shows a series of vortices rolling along the southern edge in the HR model. These are not present in the LR model and are more diffuse in the MR model, but do include a distinct region og flow from the lagoon region in a south-easterly direction into the eddy. The video in the supplementary information demonstrates a full tidal cycle for the HR model. At high tide the flow is also lower within the One Tree lagoon in the HR models, compared to both the MR, and especially the LR model.

Further away from OTR also shows changes in flow. The top north-west corner of the plots (Heron Island) shows subtle differences despite the resolution of the models being very similar this distance from OTR. Similarly, the southern edges of all plots show subtle differences in flow across resolution as a direct consequence of differences in the flow on the southern edge of OTR, whilst the resolution here is also similar in all models.

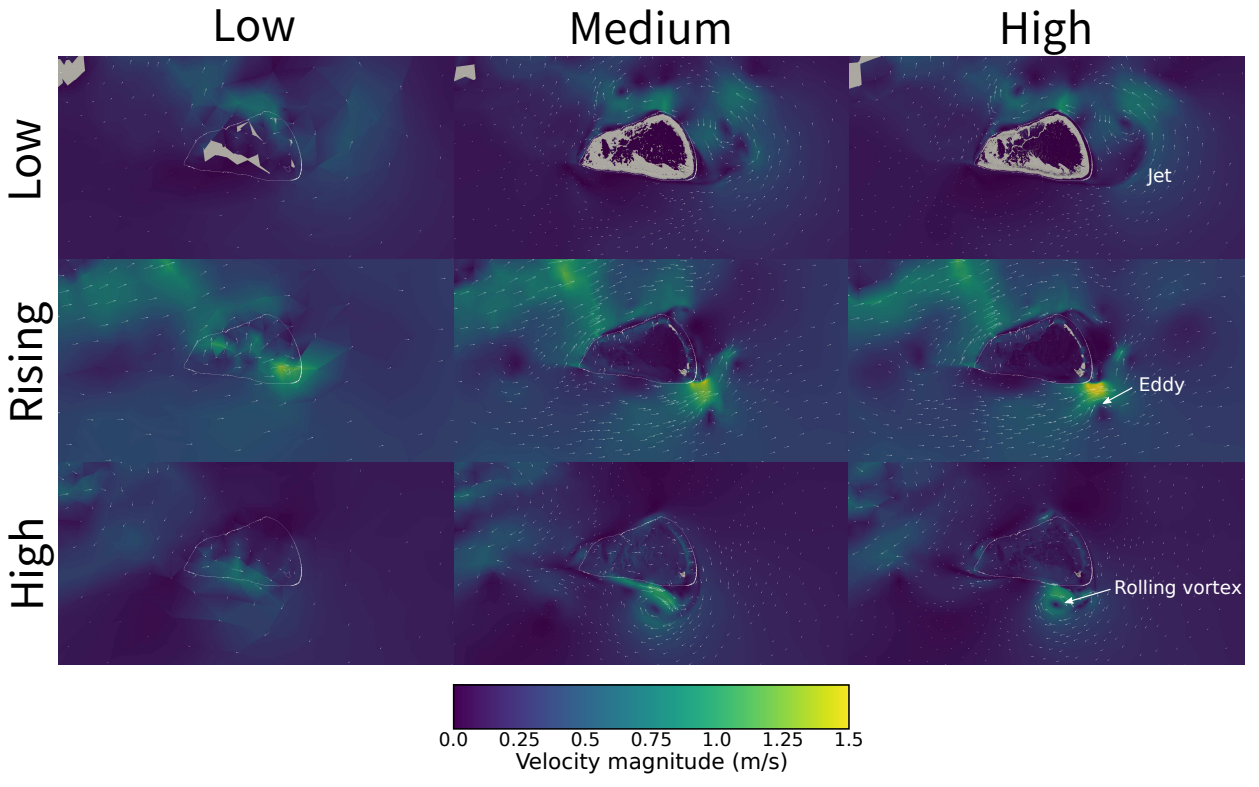

Figure 5: Comparison of the spatial velocity patterns around OTR for the three model resolution (columns) at three points in the tidal cycle (rows: low, rising and high tide) during the peak spring tide period. Arrows show directionality and are scaled to the magnitude, also shown by the colour scale. The white line is the outline of One Tree Reef for reference.

During the neap tidal period there are similar, but more subtle differences in the flow field around OTR. As with the spring tidal period, there is a clear jet and subsequent vortex shedding off the southern edge of the island in an easterly direction during low tide (Fig. 6). This appears completely absent in the LR simulation. Similarly, the western edge of OTR up toward Heron island is very similar in the MR and HR simulations with a clear flow separation visible, but is absent in the LR simulation. During rising tide (flood, with predominantly westerly flow) there are high magnitudes of flow in the lagoon for the LR simulation and a lack of eddies on along the southern edge of the reef, compared to the MR and HR simulations. At high tide there are substantial differences in the flow magnitude within the lagoon, with the LR simulation showing flow of around 0.5 m/s higher than the other two simulations. The LR simulation also lacks a clear jet structure from the western edge of the island, which is visible in the other simulations.

3.3. Impact of resolution on lagoon flushing

The differences in flow regime then impact how the water within the lagoon is exchanged with the open ocean. Counting the number of particles that are within the lagoon area shows that the LR simulations take around 5 days to go from 10,000 particles to 1,000 during the spring tide phase (Fig. 7A). In contrast the MR simulations take around 15 days on average and the HR simulations 23 days. The variation in counts is also higher in the MR and HR simulations and some of these simulations show substantial increases in particles within the lagoon at times. Animations of the particle experiments show that the LR simulation particles stay in relatively coherent groups after the initial flushing from the lagoon (see supplementary information). There are only a small number of particles left in the lagoon after the first few hours. In contrast the HR simulation shows that particles remain within the low velocity area of the lagoon,

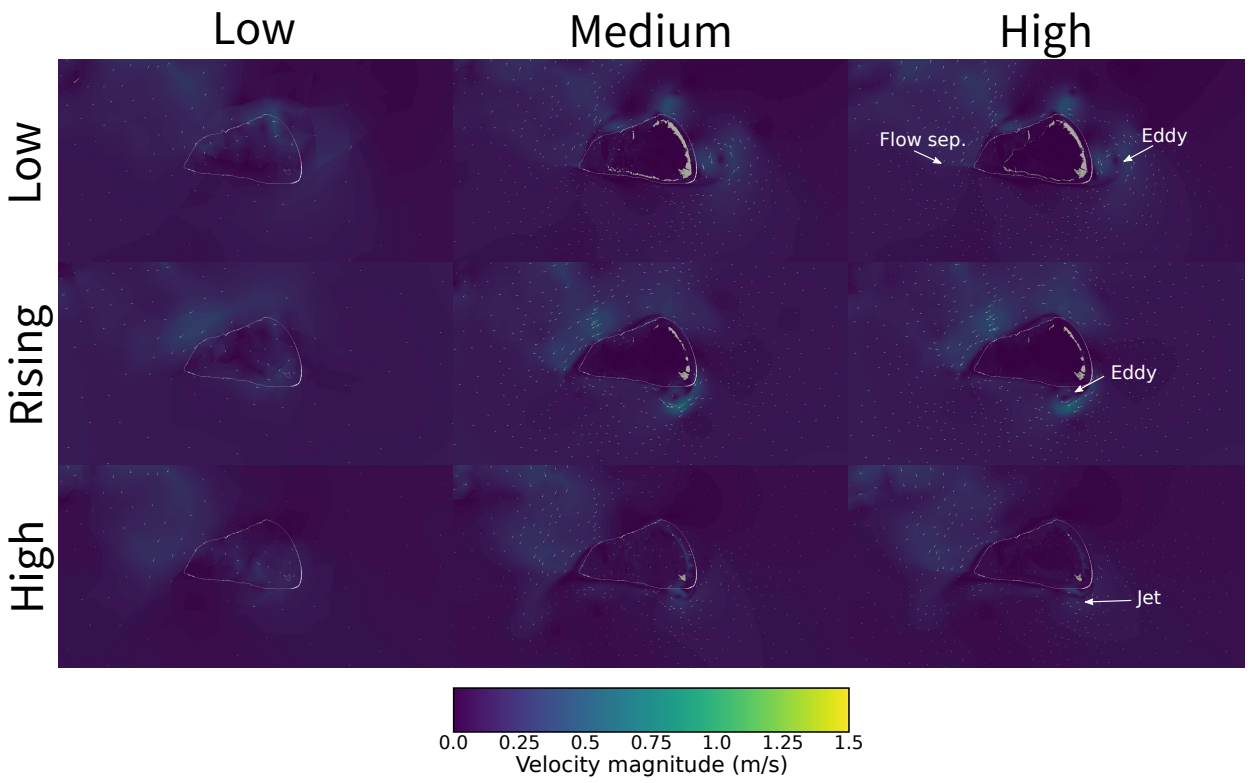

Figure 6: As Fig. 5 but for the neap phase of the tidal cycle.

flushing out along specific pathways. Flow is severely inhibited within the lagoon, meaning particles stay there for a much longer period in time with flushing into the open ocean further inhibited by the low tide creating a barrier. The MR simulation shows a lot of similarities with the HR simulation, but higher flow in the initial stages leads to an immediate flushing of a large number of particles. However, this is clearly a function of the release point as over the 16 spring tide releases the mean initial loss of particles is very similar to the high resolution simulation (Fig. 7A).

The neap period shows a much decreased flushing rate in all simulations, but similar differences are seen between the three model resolutions. The LR run takes until around 31 hours to go from 10,000 to 1,000 particles. Neither the MR or HR simulations reach 1,000 particles in the lagoon over the 2 day particle tracking experiment. The LR simulations show much greater variability (shaded area, Fig. 7) in flushing rates for the first 20 hours compared to the spring tide simulations, whereas the MR and HR simulations show similar variation as a function of release time. Videos in the supplementary information show the particle through time for each 2 day experiment.

The flushing rates compared over the 16 simulations of neap and spring tide respectively, show different impacts of resolution on the flushing rate. The three model resolutions show significant differences ($p < 0.001$) for the majority of the neap tidal cycle, with MR-HR demonstrating no statistically significant differences for the the first 10 hours (Table 3). The next 10 hours show significant differences at $p < 0.05$ (15 hours) and $p < 0.01$ (20 hours) and all subsequent hours are significantly different to $p < 0.001$. Similar MR-LR are significantly different to $p < 0.01$ for hours 5 and 10, before being significantly different to $p < 0.001$ for the remainder of the tidal cycle. These results are confirmed by the functional ANOVA analysis, with statistically significant differences between all three models using both test methods (Table 4). The spring tidal cycles is more complex. The MR-LR comparison shows statistically significant differences ($p < 0.001$) for the first 10 hours, but then all comparisons are not statistically significantly different for the remainder of the tidal cycle (Table 3). However, the functional ANOVA results show statistically significant differences for all tests for the MR-LR comparison (Table 4). The HR-LR comparison is significantly different (to varying p-values) throughout the cycle, except for the final time (45 hours). The functional ANOVA shows a significant difference for all tests. Finally, the MR-HR resolution difference shows no significant difference at hour 5, followed by significant difference (at varying p-values) for hours 10 to 35, followed by no significant differences for the final two time outputs

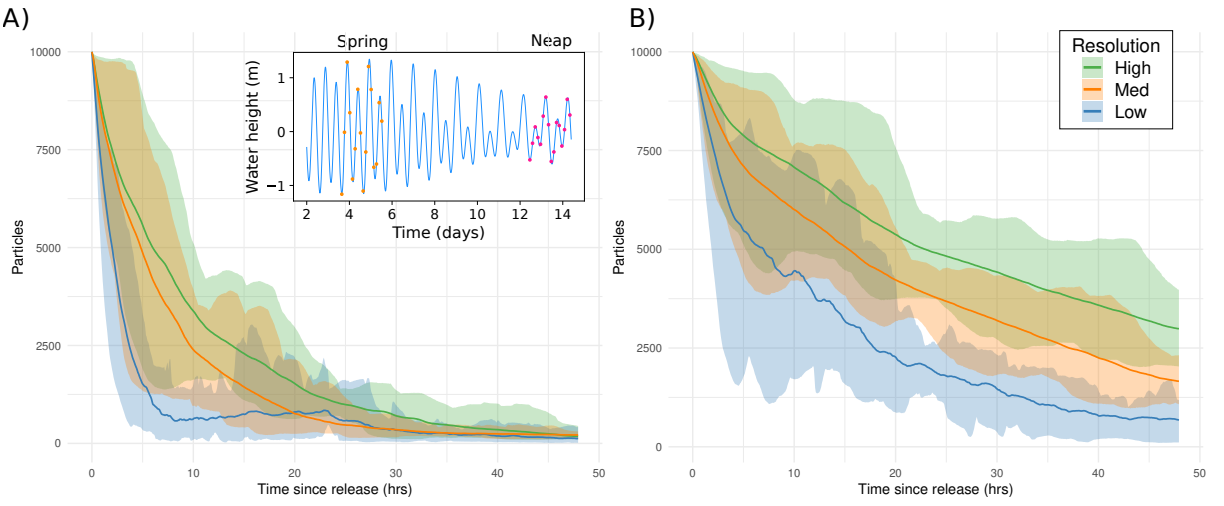

Figure 7: Number of particles within the OTR area from time of release (10,000 particles) over a 48 hour period for each release (shaded areas) and the mean (solid line) for the spring tidal period (A) and neap (B). Colour denotes the model resolution. The inset graph shows the release times against model elevation - orange dots denote spring tide releases and red show neap tide releases.

Table 3
Difference in the mean values of the number of particles within OTR at 5 hourly intervals. The model comparison is in the leftmost column, i.e. 'LR-HR' denotes the high resolution model mean was subtracted from the low resolution model mean. Colour intensity indicates significance threshold: white is not significant, lightest green is $p < 0.05$, middle green is $p < 0.01$ and darkest green is $p < 0.001$.

Neap	5	10	15	20	25	30	35	40	45
LR-HR	-2403.9	-2625.3	-2983.6	-2625.3	-2625.3	-2625.3	-2897.6	-2625.3	-2446.0
MR-HR	-774.6	-1071.6	-1100.7	-1150.2	-1143.7	-1225.3	-1246.3	-1333.4	-1363.3
MR-LR	1629.3	1629.3	1629.3	1954.9	1891.4	1730.4	1651.3	1467.5	1082.7
Spring									
LR-HR	-4057.9	-2754.3	-1550.9	-724.3	-410.5	-365.1	-217.1	-159.7	-97.1
MR-HR	-705.9	-987.5	-853.5	-768.1	-521.9	-352.9	-204.7	-108.1	-17.8
MR-LR	3351.9	1766.8	697.4	-43.9	-111.4	12.1	12.4	51.6	79.4

(Table 3). The functional ANOVA shows a mix of significant (TRP tests to $p < 0.05$) and non-significant (L2N test) results (Table 4).

The paths taken by particles show substantial differences in exit locations depending on resolution. Generally, the LR simulations show a diffuse patterns of exit locations around most of the reef rim, with a high concentration on the south-east corner (near 'Gutter'). All models show few exit pathways across the north-east corner. As resolution increases, the exist locations become better defined. The HR simulation shows four distinct exit areas: the northern 'Notch', the eastern edge of the reef ('embryonic channel' and 'Gutter') and a channel on the southern margin ('Shark Alley') during spring conditions. In neap conditions, however, the exit locations shift slightly, with a new location to the west of 'Notch' on the northern margin (Fig. 8) The eastern edge of the reef remains a high density area, but 'Shark Alley' is no longer a clear exit point. During spring tides, the MR model shows 'Shark Alley' on the southern edge as a high density area, as well 'Notch' and 'Gutter'. However, 'embryonic channel' is not as clear as the HR model. During neap tides there is a clear shift to the northern edge of the reef as exit points. A new high density region, 'Entrance' appears (similar in location to Wilson (1985) point B) and 'Notch' becomes higher density, as does a point to the west, similar to the HR model. However, like the HR model, the south-eastern corner remains the main exit location. Finally, the LR shows much less focused exit areas, but are somewhat similar to the high resolution model at spring tide, with the addition of a westerly exit point and lower density on the northern edge. At neap tide times, the exit points are similar to the medium resolution model, with the addition of the same high density area on the far western tip of

the island as seen in the spring tide. Similar patterns are seen on entry points around the reef rim. However, notable exceptions include the lack of higher density in the area around 'Shark Alley' and 'embryonic channel' as seen in the HR model during the spring tide (Fig. 9). For all other locations, the density maps for entry and exit are similar.

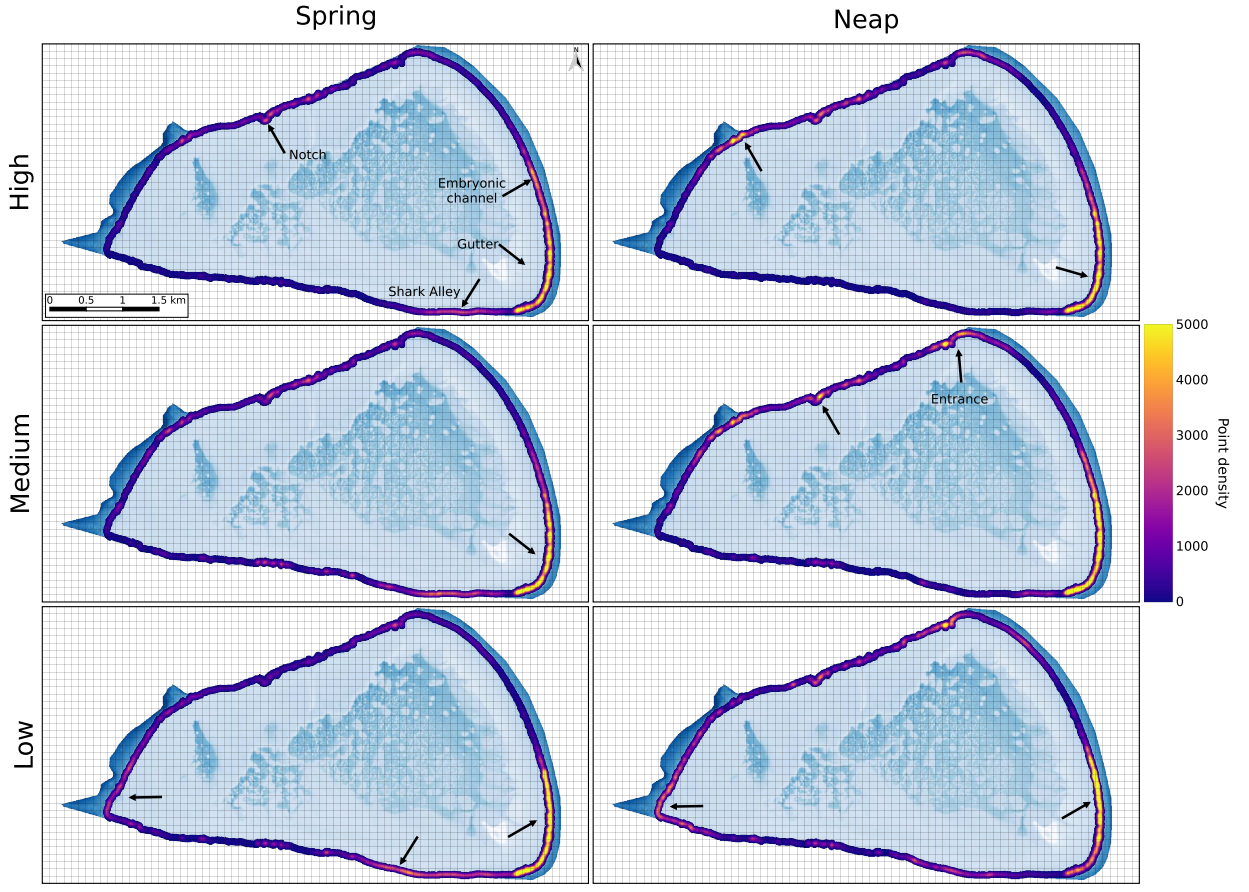

Figure 8: Density maps showing the number of particles that cross out of the OTR area at each point on a 5 x 5 m grid. Areas of note are highlighted by arrows (see text). Top row shows the high resolution model output, centre show middle resolution and the bottom shows the low resolution model output. Left is the spring tidal period, right is the neap tidal period. Bathymetry is indicated by the blue colours using the LiDAR bathymetric map with darker colours indicating deeper water. Grid lines are at 100 m intervals for reference.

4. Discussion

The results show very clear change of tidal hydrodynamics depending on the resolution of the model. In this experiment we have used the same model, same parameters and same bathymetric data and altered *only* the numerical mesh (which does mean the modelled bathymetry is different). Any changes observed are therefore due to the resolution. However, this does not necessarily mean the higher resolution is more accurate or correct in any sense of those words. Here, we have demonstrated that the higher resolution model does replicate known tidal phenomenon on OTR; namely the asymmetric filling and emptying of the lagoon as measured by Wilson (1985). It is possible that the lower resolution models could be tuned to replicate this aspect more faithfully, but this was not attempted in this work. Moreover, it is beyond the scope of this work to compare our model to satellite images in the region to compare the hydrodynamic flow structures seen in the model.

The change in resolution causes clear, and well defined, changes in flow patterns; this is more evident where wetting and drying is a major factor. The low resolution simulations do not capture the shape of OTR's reef around the island, with clear channels and spur and groove formations 'missing' in the bathymetry when interpolated onto the mesh.

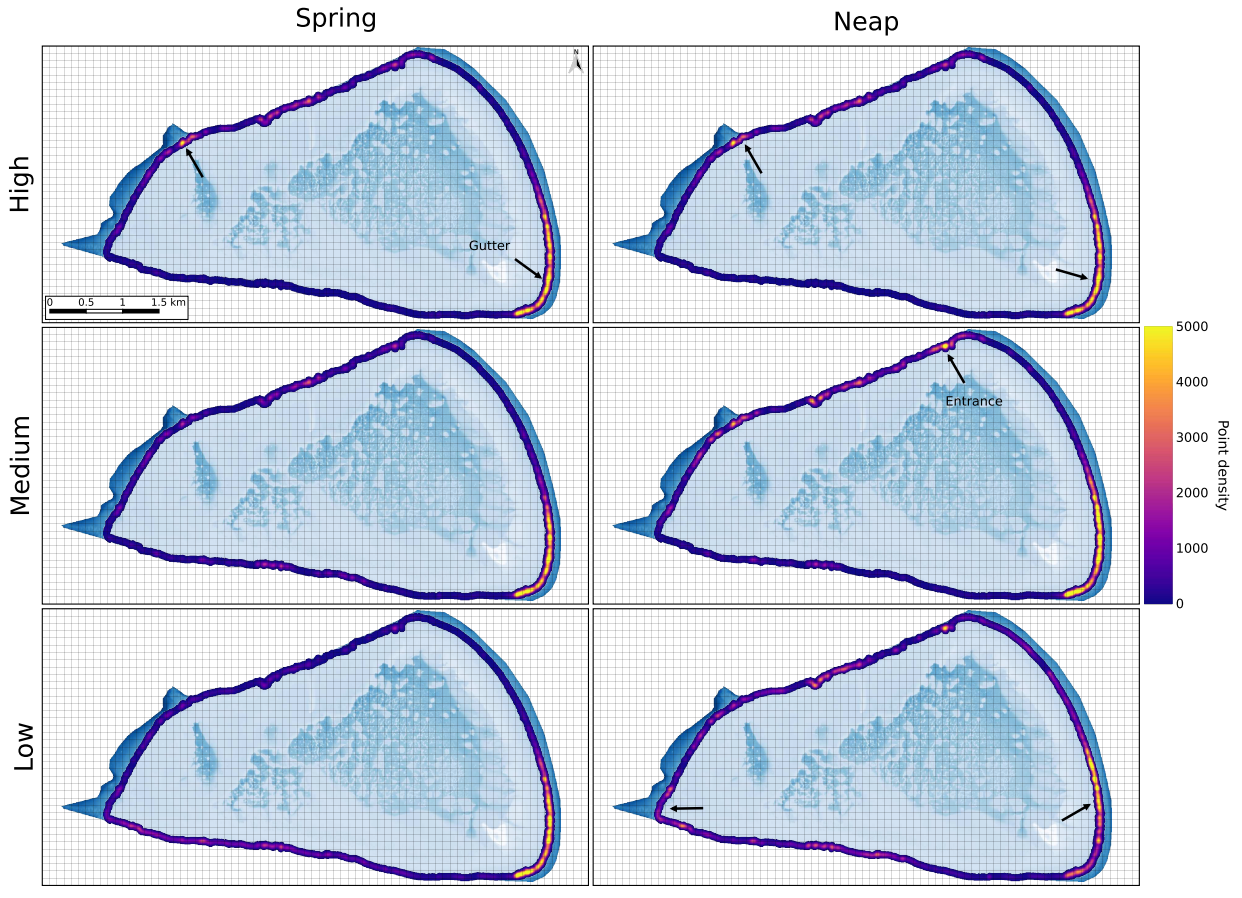

Figure 9: Density maps showing the number of particles that cross into of the OTR area at each point on a 5 x 5 m grid. Areas of note are highlighted by arrows (see text). See Fig 8 for further details.

Table 4
Results form the Functional Data Analysis ANOVA tests represented as p-values for each model pair combination and the two tests used to compare the 16 groups of flushing rate time series per model.

	L2N	TRP		
Neap		ANOVA	ATS	WTPS
LR-HR	$p < 0.001$	$p < 0.001$	$p < 0.001$	$p < 0.001$
MR-HR	$p < 0.001$	$p < 0.001$	$p < 0.001$	$p < 0.001$
MR-LR	$p < 0.001$	$p < 0.001$	$p < 0.001$	$p < 0.001$
Spring				
LR-HR	$p < 0.001$	$p < 0.001$	$p < 0.001$	$p < 0.001$
MR-HR	$p = 0.052$	$p = 0.024$	$p = 0.017$	$p = 0.027$
MR-LR	$p < 0.001$	$p < 0.001$	$p < 0.001$	$p < 0.001$

This then inhibits the ponding effect and hence the lack of simulation of this physical phenomenon. In turn, this means additional analyses that depend on the flow, here lagoon flushing, but also analyses like coral larval connectivity, would be potentially flawed. The medium resolution (~50 m) appeared to visually match the flow patterns well, but surprisingly was significantly different in the secondary analysis of lagoon flushing – both in terms of the rates and locations of outflow and inflow. A number of the locations where there is high outflow from the lagoon, the 'Shark Alley' and 'embryonic channel' are not highlighted in the MR and LR models. The lagoon flushing simulated here is much more rapid than at Scott Reef (Western Australia) which was simulated by Green et al. (2018) using a virtual tracer method within a 35 m resolution model using a 10 m resolution bathymetric data set. Both One Tree and Scott

Reef have similar tidal ranges (3.5 to 4 m) and semi-diurnal tides, but Green et al. (2018) included wind and wave currents, which were excluded here to focus on tidal dynamics only. Simulating Scott Reef at extreme resolution or One Tree with wind and wave currents would allow a more direct comparison.

All of the resolutions chosen here would all be considered as 'high' resolution in many modelling domains; Saint-Amand et al. (2023) stated that to model the Great Barrier Reef with any clarity of the reef matrix and rapid changes in bathymetry, a resolution of 250 - 500 m is required. Here, the lowest resolution was 250 m, so around that recommended by Saint-Amand et al. (2023). However, this resolution does not fully capture the tidal dynamics in and around a coral atoll like OTR. It is clear that wetting and drying processes are crucial to the simulation of the atoll and these are largely lost in the low resolution model. One Tree Island is around 200 m across and 400 m in the longest dimension so is not fully captured in the LR model. Once the model has sufficient resolution, the flow regime is more fully captured around the island. However, despite the similarities of the flow between the medium and high resolution models, the differences that do exist then produce statistically significant differences in secondary analysis that depend on the flow. This then explains previous studies that have examined fish egg and larval dispersal on OTR. Burgess et al. (2007) simulated the hydrodynamics around OTR, using a 300 m model, and captured the two large-scale eddies that form in the lee of the island on both the ebb and flood tides ('phase eddies'). However, their distribution of fish capture shows large numbers on the southern edge of OTR on both ebb and flood tides (their figure 3) which matches the 'rolling eddies' simulated in the medium and high resolution models presented here. Similarly, Booth et al. (2000) show that 'Shark Alley' is a location of high larval settlement. Booth et al. (2000) hypothesis that this is due to the connection between the lagoon and ocean, but other sites ('Entrance' and 'Gutter') have similar geomorphological features, but were not sites of high recruitment. Here, we show that lagoon flushing pathways are concentrated around 'Shark Alley' during the spring tide and 'Gutter' during neap tide (Fig. 8). The high resolution tidal model can therefore explain this and also explain why Burgess et al. (2007) could not see these phenomenon in their 300 m resolution model. More widely, using different hydrodynamic models has shown to produce difference in particle tracking outcomes Choukroun et al. (2025). Adding wave processes to the model presented here may change some of these conclusions and will be investigated in future. The predominant wave and wind direction on OTR is from the south-east Perris et al. (2024), so the main entry points on the eastern edge of the reef will likely be the same, but there may be fewer exit points on the eastern edge. We also anticipate the entry and exit points to become more diffuse when wind and waves are added due to the temporal variability in wind direction.

The advent of digital twinning requires a thorough understanding of the physical processes that are resolvable within any numerical framework developed. Depending on the aim of the digital twin platform, for example simulating the impacts of coastal engineering, impacts of storms over a wide area, or examining changes in sea-surface height over an ocean, will require a different requirement in terms of resolution. This has been well known for numerical models for a long time, but is worth repeating as we move to digital twin platforms. These issues may be of larger consequence, depending on the pipeline used to create the digital twin. For example, a pipeline like that described in Chattopadhyay et al. (2024), which is a neural network trained on satellite data cannot, by definition, make predictions at a finer scale than that of the training data nor should it predict anything beyond the limits seen in the training data. To put it another way, we should not trust a prediction that is at a higher resolution than that of the training data or predicts events beyond those seen in the training data. A complication occurs when the training data is a mix of resolutions – what do we take as the effective resolution of such a model? Adding different numerical models at a range of resolutions into the training data may mitigate these concerns as they will then encompass the range of reasonable (assuming the models are well validated and verified) outcomes. In addition, any numerical model will add a physical/chemical/biological mathematical framework, and as shown here, resolution is an important consideration in that training. However, there also needs to be caution in terms of the assumptions made in any numerical model and if those assumptions are being violated in pushing model resolution toward that of available data, such as satellite or bathymetric data. In such cases, multi-model frameworks may be required, coupling unstructured mesh models with higher resolution, three-dimensional models, in areas of interest. Work, such as that here, needs to be carried out to explore the boundaries of what is possible, balancing the data, artificial intelligence and physical numerical modelling components of any digital twin.

5. Conclusions

Model resolution has long known to be a source of error in numerical models of ocean and coastal processes. The creation of digital twins on either data alone or a mix of numerical models and data creates new issues, but the issue of

model resolution still remains, particularly with the advancement of extremely high resolution data. Here, we examine what physical processes are revealed as we move from good resolution (250 m) to extreme resolution (5 m) within an unstructured mesh tidal model in a complex, coral reef atoll environment. We show that only the very high resolution can correctly simulate the ponding effect observed at this location. The differences in flow are largely due to correctly simulating the wetting and drying around the atoll rim, which in turn dictate the pathways of water exchange on and off the atoll. At ultra-high resolution fine scale eddies ('rolling eddies') form as part of the ebb and flood cycle on the southern edge of the atoll. These in turn give a coherence to water parcels which can explain observations of fish egg and larvae distributions from previous studies. As we move from numerical modelling to digital twins, resolution of both the training data and any training model must be a consideration on what processes can be seen in the final outputs.

6. Data and videos

Model inputs and processing scripts are available on github: `https://github.com/EnvModellingGroup/oti_resolution`.

Videos of model outputs are available on Figshare, DOI: 10.6084/m9.figshare.30110200

7. Acknowledgements

This project was undertaken on the Viking Cluster, which is a high performance compute facility provided by the University of York. We are grateful for computational support from the University of York High Performance Computing service, Viking and the Research Computing team. This work was supported by the Natural Environment Research Council (NERC) and the Adapting to the Challenges of a Changing Environment (ACCE) Doctoral Training Partnership (NE/S00713X/1). We thank three anonymous reviewers for their comments and suggestions to improve the manuscript.

References

Alsulaiman, N., van Reeuwijk, M., Piggott, M.D., 2025. Impact of data assimilation frequency and observation location in thermal effluent modeling for coastal waters. Earth and Space Science (Hoboken, N.J.) 12, e2024EA004099. doi:10.1029/2024ea004099.

Andutta, F.P., Kingsford, M.J., Wolanski, E., 2012. 'Sticky water' enables the retention of larvae in a reef mosaic. Estuarine, coastal and shelf science 101, 54–63. doi:10.1016/j.ecss.2012.02.013.

Angeloudis, A., Kramer, S.C., Avdis, A., Piggott, M.D., 2018. Optimising tidal range power plant operation. Applied Energy 212, 680–690. doi:10.1016/j.apenergy.2017.12.052.

Avdis, A., Candy, A.S., Hill, J., Kramer, S.C., Piggott, M.D., 2018. Efficient unstructured mesh generation for marine renewable energy applications. Renewable Energy 116, 842–856. doi:10.1016/j.renene.2017.09.058.

Baker, A.L., Craighead, R.M., Jarvis, E.J., Stenton, H.C., Angeloudis, A., Mackie, L., Avdis, A., Piggott, M.D., Hill, J., 2020. Modelling the impact of tidal range energy on species communities. Ocean & Coastal Management 193, 105221. doi:10.1016/j.ocecoaman.2020.105221.

Balay, S., Buschelman, K., Gropp, W.D., Kaushik, D., Knepley, M.G., McInnes, L.C., Smith, B.F., Zhang, H., 2001. Petsc. See http://www. mcs. anl. gov/petsc .

Bauder, Y., Mamo, B., Brock, G.A., Kosnik, M.A., 2023. One Tree Reef Foraminifera: a relic of the pre-colonial Great Barrier Reef. Geological Society special publication 529, 175–193. doi:10.1144/sp529-2022-64.

Beaman, R.J., 2010. 3DGBR: A high-resolution depth model for the Great Barrier Reef and Coral Sea. Marine and Tropical Sciences Facility (MTSRF) Project 2.

Black, K.P., Gay, S.L., 1987. Eddy formation in unsteady flows. Journal of Geophysical Research: Oceans 92, 9514–9522. doi:10.1029/JC092iC09p09514.

Bode, L., Mason, L.B., Middleton, J.H., 1997. Reef parameterisation schemes with applications to tidal modelling. Progress in oceanography 40, 285–324. doi:10.1016/s0079-6611(98)00006-8.

Booth, D.J., Kingsford, M.J., Doherty, P.J., Beretta, G.A., 2000. Recruitment of damselfishes in One Tree Island lagoon: persistent interannual spatial patterns. Marine ecology progress series 202, 219–230. doi:10.3354/meps202219.

Burgess, S.C., Kingsford, M.J., Black, K.P., 2007. Influence of tidal eddies and wind on the distribution of pre-settlement fishes around One Tree Island, Great Barrier Reef. Marine ecology progress series 341, 233–242. doi:10.3354/meps341233.

Chattopadhyay, A., Gray, M., Wu, T., Lowe, A.B., He, R., 2024. OceanNet: a principled neural operator-based digital twin for regional oceans. Scientific reports 14, 21181. doi:10.1038/s41598-024-72145-0.

Choukroun, S., Stewart, O.B., Mason, L.B., Bode, M., 2025. Larval dispersal predictions are highly sensitive to hydrodynamic modelling choices. Coral reefs 44, 1–13. doi:10.1007/s00338-024-02563-z.

Cummins, P.F., Thupaki, P., 2017. A note on evaluating model tidal currents against observations. Continental Shelf Research 152, 35–37. doi:10.1016/j.csr.2017.10.007.

Davies, P.J., Radke, B.M., Robison, C.R., 1976. The evolution of One Tree Reef, southern Great Barrier Reef, Queensland. AGSO journal of Australian geology & geophysics 1, 231–240.

Delandmeter, P., van Sebille, E., 2019. The Parcels v2.0 Lagrangian framework: new field interpolation schemes. Geoscientific model development 12, 3571–3584. doi:10.5194/gmd-12-3571-2019.

Duce, S., Vila-Concejo, A., McCarroll, R.J., Yiu, B., Perris, L.A., Webster, J.M., 2022. Field measurements show rough fore reefs with spurs and grooves can dissipate more wave energy than the reef crest. Geomorphology 413, 108365. doi:10.1016/j.geomorph.2022.108365.

Durden, J.M., 2025. Environmental management using a digital twin. Environmental science & policy 164, 104018. doi:10.1016/j.envsci.2025.104018.

Eddy, T.D., Lam, V.W.Y., Reygondeau, G., Cisneros-Montemayor, A.M., Greer, K., Palomares, M.L.D., Bruno, J.F., Ota, Y., Cheung, W.W.L., 2021. Global decline in capacity of coral reefs to provide ecosystem services. One earth (Cambridge, Mass.) 4, 1278–1285. doi:10.1016/j.oneear.2021.08.016.

Egbert, G.D., Erofeeva, S.Y., 2002. Efficient inverse modeling of barotropic ocean tides. Journal of Atmospheric and Oceanic Technology 19, 183–204.

Elmhirst, T., Connolly, S.R., Hughes, T.P., 2009. Connectivity, regime shifts and the resilience of coral reefs. Coral reefs 28, 949–957. doi:10.1007/s00338-009-0530-8.

Frith, C.A., Mason, L.B., 1986. Modelling wind driven circulation One Tree Reef, Southern Great Barrier Reef. Coral reefs 4, 201–211. doi:10.1007/bf00298078.

GDAL/OGR contributors, 2025. GDAL/OGR Geospatial Data Abstraction software Library.

Geuzaine, C., Remacle, J.F., 2009. Gmsh: A 3-D finite element mesh generator with built-in pre- and post-processing facilities. International journal for numerical methods in engineering 79, 1309–1331. doi:10.1002/nme.2579.

Green, R.H., Lowe, R.J., Buckley, M.L., 2018. Hydrodynamics of a tidally forced coral reef atoll. Journal of Geophysical Research, C: Oceans 123, 7084–7101. doi:10.1029/2018jc013946.

Greenberg, D.A., Dupont, F., Lyard, F.H., Lynch, D.R., Werner, F.E., 2007. Resolution issues in numerical models of oceanic and coastal circulation. Continental shelf research 27, 1317–1343.

Gruber, R.K., Lowe, R.J., Falter, J.L., 2017. Metabolism of a tide-dominated reef platform subject to extreme diel temperature and oxygen variations: Metabolism of a tide-dominated reef platform. Limnology and oceanography 62, 1701–1717. doi:10.1002/lno.10527.

Górecki, T., Smaga, L., 2019. fdANOVA: an R software package for analysis of variance for univariate and multivariate functional data. Computational statistics 34, 571–597. doi:10.1007/s00180-018-0842-7.

Harker, A., Green, J.A.M., Schindelegger, M., Wilmes, S.B., 2019. The impact of sea-level rise on tidal characteristics around Australia. Ocean Science 15, 1. doi:10.5194/os-15-147-2019.

Harris, D.L., Vila-Concejo, A., Webster, J.M., 2014. Geomorphology and sediment transport on a submerged back-reef sand apron: One Tree Reef, Great Barrier Reef. Geomorphology 222, 132–142. doi:10.1016/j.geomorph.2014.03.015.

Harris, D.L., Webster, J.M., Vila-Concejo, A., Duce, S., Leon, J.X., Hacker, J., 2023. Defining multi-scale surface roughness of a coral reef using a high-resolution LiDAR digital elevation model. Geomorphology (Amsterdam, Netherlands) 439, 108852. doi:10.1016/j.geomorph.2023.108852.

Hatcher, A.I., Frith, C.A., 1985. The control of nitrate and ammonium concentrations in a coral reef lagoon. Coral reefs 4, 101–110. doi:10.1007/bf00300868.

Hazeleger, W., Aerts, J.P.M., Bauer, P., Bierkens, M.F.P., Camps-Valls, G., Dekker, M.M., Doblas-Reyes, F.J., Eyring, V., Finkenauer, C., Grundner, A., Hachinger, S., Hall, D.M., Hartmann, T., Iglesias-Suarez, F., Janssens, M., Jones, E.R., Kölling, T., Lees, M., Lhermitte, S., van Nieuwpoort, R.V., Pahker, A.K., Pellicer-Valero, O.J., Pijpers, F.P., Siibak, A., Spitzer, J., Stevens, B., Vasconcelos, V.V., Vossepoel, F.C., 2024. Digital twins of the Earth with and for humans. Communications earth & environment 5, 1–11. doi:10.1038/s43247-024-01626-x.

Hill, J., 2019. HRDS: A Python package for hierarchical raster datasets. Journal of Open Source Software 4, 1112. doi:10.21105/joss.01112.

Hill, J., Rush, G., Peakall, J., Johnson, M., Hodson, L., Barlow, N.L.M., Bowman, E.T., Gehrels, W.R., Hodgson, D.M., Kesserwani, G., 2023. Resolving tsunami wave dynamics: Integrating sedimentology and numerical modelling. The depositional record doi:10.1002/dep2.247.

Hoegh-Guldberg, O., Mumby, P.J., Hooten, A.J., Steneck, R.S., Greenfield, P., Gomez, E., Harvell, C.D., Sale, P.F., Edwards, a.J., Caldeira, K., Knowlton, N., Eakin, C.M., Iglesias-Prieto, R., Muthiga, N., Bradbury, R.H., Dubi, A., Hatziolos, M.E., 2007. Coral Reefs Under Rapid Climate Change and Ocean Acidification. Science 318, 1737–1742. doi:10.1126/science.1152509.

Kärnä, T., De Brye, B., Gourgue, O., Lambrechts, J., Comblen, R., Legat, V., Deleersnijder, E., 2011. A fully implicit wetting–drying method for DG-FEM shallow water models, with an application to the Scheldt Estuary. Computer Methods in Applied Mechanics and Engineering 200, 509–524.

Kärnä, T., Kramer, S.C., Mitchell, L., Ham, D.A., Piggott, M.D., Baptista, A.M., 2018. Thetis coastal ocean model: discontinuous Galerkin discretization for the three-dimensional hydrostatic equations. Geoscientific Model Development 11, 4359–4382.

Kosnik, M.A., Hua, Q., Kaufman, D.S., Zawadzki, A., 2015. Sediment accumulation, stratigraphic order, and the extent of time-averaging in lagoonal sediments: a comparison of 210Pb and 14C/amino acid racemization chronologies. Coral reefs 34, 215–229. doi:10.1007/s00338-014-1234-2.

Kutser, T., Hedley, J., Giardino, C., Roelfsema, C., Brando, V.E., 2020. Remote sensing of shallow waters – A 50 year retrospective and future directions. Remote sensing of environment 240, 111619. doi:10.1016/j.rse.2019.111619.

Lee, K.C., Webster, J.M., Salles, T., Mawson, E.E., Hill, J., 2022. Tidal dynamics drive ooid formation in the Capricorn Channel since the Last Glacial Maximum. Marine geology 454, 106944. doi:10.1016/j.margeo.2022.106944.

Ludington, C.A., 1979. Tidal Modifications and Associated Circulation in a Platform Reef Lagoon. Marine and Freshwater Research 30, 425–430. doi:10.1071/mf9790425.

Mawson, E.E., Lee, K.C., Hill, J., 2022. Sea level rise and the Great Barrier Reef the future implications on reef tidal dynamics. Journal of Geophysical Research, C: Oceans doi:10.1029/2021jc017823.

McCarthy, M.J., Otis, D.B., Hughes, D., Muller-Karger, F.E., 2022. Automated high-resolution satellite-derived coastal bathymetry mapping. International journal of applied earth observation and geoinformation: ITC journal 107, 102693. doi:10.1016/j.jag.2022.102693.

Osorio-Cano, J.D., Alcérreca-Huerta, J.C., Osorio, A.F., Oumeraci, H., 2018. CFD modelling of wave damping over a fringing reef in the Colombian Caribbean. Coral Reefs 37, 1093–1108. doi:10.1007/s00338-018-1736-4.

Perris, L., Salles, T., Fellowes, T.E., Duce, S., Webster, J., Vila-Concejo, A., 2024. The influence of coral reef spur and groove morphology on wave energy dissipation in contrasting reef environments. Journal of geophysical research. Earth surface 129, e2023JF007424. doi:10.1029/2023jf007424.

QGIS.org, 2020. QGIS Geographic Information System. Open Source Geospatial Foundation Project.

Rogers, J.S., Monismith, S.G., Dunbar, R.B., Koweek, D., 2015. Field observations of wave-driven circulation over spur and groove formations on a coral reef. Journal of Geophysical Research. Oceans 120, 145–160. doi:10.1002/2014jc010464.

Saint-Amand, A., Lambrechts, J., Thomas, C.J., Hanert, E., 2023. How fine is fine enough? Effect of mesh resolution on hydrodynamic simulations in coral reef environments. Ocean Modelling , 102254doi:10.1016/j.ocemod.2023.102254.

da Silva, R.F., Storlazzi, C.D., Rogers, J.S., Reyns, J., McCall, R., 2020. Modelling three-dimensional flow over spur-and-groove morphology. Coral reefs 39, 1841–1858. doi:10.1007/s00338-020-02011-8.

Talavera, L., Vila-Concejo, A., Webster, J.M., Smith, C., Duce, S., Fellowes, T.E., Salles, T., Harris, D., Hill, J., Figueira, W., Hacker, J., 2021. Morphodynamic Controls for Growth and Evolution of a Rubble Coral Island. Remote Sensing 13, 1582. doi:10.3390/rs13081582.

Tlhomole, J.B., Alosairi, Y., Hughes, G.O., Piggott, M.D., 2025. Measuring marine hydrodynamics from space using planet satellite imagery. Remote sensing of environment 324, 114741. doi:10.1016/j.rse.2025.114741.

Torres-Pulliza, D., Dornelas, M.A., Pizarro, O., Bewley, M., Blowes, S.A., Boutros, N., Brambilla, V., Chase, T.J., Frank, G., Friedman, A., Hoogenboom, M.O., Williams, S., Zawada, K.J.A., Madin, J.S., 2020. A geometric basis for surface habitat complexity and biodiversity. Nature ecology & evolution 4, 1495–1501. doi:10.1038/s41559-020-1281-8.

Tzachor, A., Hendel, O., Richards, C.E., 2023. Digital twins: a stepping stone to achieve ocean sustainability? npj Ocean Sustainability 2, 1–8. doi:10.1038/s44183-023-00023-9.

Vila-Concejo, A., Hamylton, S.M., Webster, J.M., Duce, S.J., Fellowes, T.E., 2022. Lagoon infilling by coral reef sand aprons as a proxy for carbonate sediment productivity. Geology 50, 1427–1431. doi:10.1130/g50453.1.

Wagner, G.L., Silvestri, S., Constantinou, N.C., Ramadhan, A., Campin, J.M., Hill, C., Chor, T., Strong-Wright, J., Lee, X.K., Poulin, F., Souza, A., Burns, K.J., Marshall, J., Ferrari, R., 2025. High-level, high-resolution ocean modeling at all scales with Oceananigans. arXiv [physics.ao-ph] arXiv:2502.14148.

Watanabe, M., Kan, H., Toguchi, K., Nakashima, Y., Roeber, V., Arikawa, T., 2023. Effect of the structural complexity of a coral reef on wave propagation: A case study from Komaka Island, Japan. Ocean Engineering 287, 115632. doi:10.1016/j.oceaneng.2023.115632.

Williamson, D.H., Harrison, H.B., Almany, G.R., Berumen, M.L., Bode, M., Bonin, M.C., Choukroun, S., Doherty, P.J., Frisch, A.J., Saenz-Agudelo, P., Jones, G.P., 2016. Large-scale, multidirectional larval connectivity among coral reef fish populations in the Great Barrier Reef Marine Park.

Molecular ecology 25, 6039–6054. doi:10.1111/mec.13908.
Wilson, P.R., 1985. Tidal studies in the One Tree Island lagoon. Marine and Freshwater Research 36, 139–156. doi:10.1071/mf9850139.
Wolanski, E., De Le Court, M., Lambrechts, J., Kingfsord, M., 2024. Mechanisms enabling the self-recruitment of passive larvae in the Great Barrier Reef. Estuarine, coastal and shelf science 309, 108976. doi:10.1016/j.ecss.2024.108976.
Wolanski, E., Drew, E., Abel, K.M., O'Brien, J., 1988. Tidal jets, nutrient upwelling and their influence on the productivity of the alga Halimeda in the Ribbon Reefs, Great Barrier Reef. Estuarine, coastal and shelf science 26, 169–201. doi:10.1016/0272-7714(88)90049-2.
Wolanski, E., Spagnol, S., 2000. Sticky waters in the Great Barrier reef. Estuarine, coastal and shelf science 50, 27–32.
Zhang, Y.J., Fernandez-Montblanc, T., Pringle, W., Yu, H.C., Cui, L., Moghimi, S., 2023. Global seamless tidal simulation using a 3D unstructured-grid model (SCHISM v5.10.0). Geoscientific model development 16, 2565–2581. doi:10.5194/gmd-16-2565-2023.